Electron transfer in keV-energy $^4He^{++}$ collisions. II. Formation of $^4He^+(2s)$ in collisions with He, Ar, H_2, and N_2†

G. A. Khayrallah* and J. E. Bayfield
J. W. Gibbs Laboratory, Physics Department, Yale University, New Haven, Connecticut, 06520
(Received 24 June 1974)

Cross sections for single-electron transfer forming the metastable state $^4He^+(2s)$ have been measured for a $^4He^{++}$ beam incident on thin He, Ar, H_2, and N_2 gas targets. The $^4He^{++}$ energy range was 7–70 keV. The experiments utilized detection of the $2s$ state via a delayed time coincidence between a field-induced Lyman-α photon and the ion itself. While the measured cross sections are believed accurate to $\pm$ 35%, they are three times larger than the recent cross sections of Shah and Gilbody using incident $^3He^{++}$ ions. The present time-coincidence technique directly measured the fraction of the total electron-transfer cross section resulting in metastable production with results ranging between 5% and 17%.

I. INTRODUCTION

The production of beams of excited ions, atoms, and molecules is receiving increased attention as the result of a number of present and future applications. In particular, electron-transfer processes can be selected that favor excited-state production over direct population of the ground state. This has led to the successful construction of intense sources of polarized protons based upon the favored production of hydrogen atoms in the $n=2$ states during keV-energy H^+ collisions with cesium vapor.[1] The present paper (II) presents data relevant to an extension of this idea to polarized ^3He sources using $^3He^{++}$ electron transfer in a gas target.[2] As discussed in paper I,[3] now the $n=2$ states of He^+ are favored because their ionization potential more closely matches that of most ground-state atoms and molecules than does the tightly bound $1s$ state. Indeed, if the target atom is atomic hydrogen, as will be the case in paper III of this series, then the ground electronic state $H(1s)$ is energy degenerate with the $n=2$ states of He^+.

In addition to the polarized-nuclei application, several other fields require increased understanding of excited-state production in electron-transfer collisions. It is now believed possible to utilize such collisions as x-ray laser pumping mechanisms. The present data is directly relevant to a present attempt to produce laser action at the Lyman-α line of He^+ at 304 Å.[4] Extension of this idea to one-electron ions of higher Z is of great interest. Another future application is the production of intense beams of excited one-electron ions for precision multiphoton atomic fine-structure and Lamb-shift measurements.[5]

The above applications depend in differing degree upon the fractional population of excited states in the collision process, with production of states with $n \neq 2$ generally undesirable. The present experiments utilize an ion-photon time-coincidence detection technique that directly obtains this fraction independent of the over-all ion-detection efficiency. Thus the uncertainty in our results for the He^+ $(2s)$-production cross sections stems from two basic sources; the first is the uncertainty in our total electron-transfer cross-section values of paper I, and the second is the accuracy in the efficiency of detection of the electric-field induced Lyman-α photons characterizing the $2s$ component in the beam. This latter question is a major concern of this paper, and a complete analysis of the problem is presented. A detailed comparison is made with the recent results of Shah and Gilbody[6] for $^3He^{++}$ collisions, with the conclusion that the factor of 3 difference between their results (uncertain by a factor of 2) and the present ones (being uncertain by ±35%) is basically a matter of Lyman-α detector calibration. This has an important bearing on further discrepancies in the He^{++}-H electron-transfer data discussed in paper III. A preliminary report of the present work has been made.[7]

II. APPARATUS

A. General description of the $He^+(2s)$ experiments

A schematic diagram of the apparatus used in this part of the research is shown in Fig. 1. A $^4He^{++}$ beam was accelerated, mass analyzed, collimated, and scattered using the same apparatus as in the preceding paper I. However, analysis of the scattered beam was performed with a differing arrangement. The scattered beam first passed through a 14.04-GHz TM_{020} microwave cavity which modulated the metastable $2s$ state in the He^+ charge

component of the beam without focusing or deflecting the ion beams. The combination of two orthogonal sets "W" of two parallel transverse-electric-field plates each trimmed the phase space of the beam as necessary. Charge analysis of the scattered beam was performed after passage through the microwave cavity. The whole charge-analysis assembly "L," "M," and "N" of Fig. 1 of paper I was transplanted into the new position shown in Fig. 1 of this paper. The secondary-electron emission Faraday cup "O" intercepted only the neutral beam whenever enough voltage was applied across plates "W" to deflect and stop the ion beam before the microwave cavity. After the charge analysis region the translatable detection assembly "P" scanned the beams. Assembly "P" was modified from that used in paper I to make possible the detection of the $He^+(2s)$ metastable state as well as the dc electric field prequenching of that state. DC prequenching was used in $He^+(2s)$ angular-distribution studies; otherwise, the microwaves were used. A complete description of the apparatus contained in "P" will be given in Sec. IIC, while Sec. IIB describes the microwave cavity "Z" and the hardware connected to and associated with it. Section IID will describe the fast pulse detection electronics used in the present experiment.

The vacuum system and the differential-pumping apertures were the same as in paper I. The position of the various vacuum pumps as well as details of the vacuum chamber are also shown in Fig. 1.

B. $He^+(2s)$ prequench microwave system

The microwave cylindrical cavity was made from oxygen-free copper and was designed to operate in the TM_{020} mode at a frequency of 14.040 GHz. Theoretically $Q = 29\,000$ for the unloaded cavity. The measured over-all loaded Q of the cavity was 9500.

The cavity had an entrance hole and an exit hole of the same dimensions. These thick apertures had a diameter of 1.016 ± 0.0025 cm and a length of 1.270 ± 0.001 cm. The aperture geometry appeared to the microwaves as a tube of radius a, whose cutoff wavelength for free propagation of a TM_{mn} mode is given by

$$\lambda_c = 2\pi a/X_{mn} = c/f_c. \tag{1}$$

Since X_{01} is the smallest zero of $J_0(x)$, the lowest frequency that the tube could propagate was

$$f_c = c/\lambda_c = cX_{01}/2\pi a = 23 \text{ GHz}, \tag{2}$$

well above our operating frequency. The length of the beam-aperture tubes was about equal to the decay length of the 14.040-GHz radiation within it; this kept the cavity Q from being lowered too much by the beam apertures.

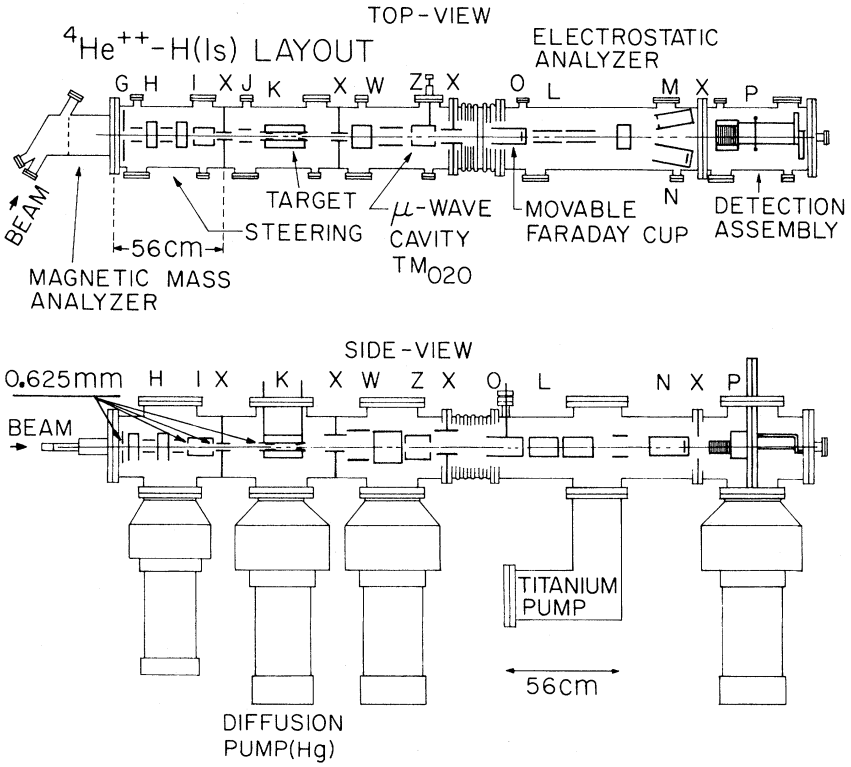

FIG. 1. Schematic diagram of the apparatus. The beam is mass analyzed, collimated at "G" and "K," scattered at the target "K," and monitored by Faraday cup "O." The $He^+(2s)$ ions are modulated by microwaves at "Z" and detected at "P."

Actually a measurement was performed to verify that the cavity was in the TM_{020} mode on resonance near 14.04 GHz. When a small sample material was inserted into the resonant cavity, the resonant frequency and the quality factor were changed by small amounts. The relationship between the change in resonant frequency and cavity volume V, cavity shape, and the properties of the perturbation sample has been investigated by several authors.[8] The shift in frequency is proportional to the square of the electric field at the sample. A 0.16-cm-diam brass ball was suspended on a nylon string and was used to map the shape of the field. The shifts in frequency were of the order of 2 MHz and were easily measured; the spatial dependence of the fields so determined was that for a TM_{020} mode. Although no detailed precision observations were made, it was also found that the fields penetrated about two ball diameters into the beam-aperture holes of the cavity.

The TM_{020} mode was chosen since in this mode the electric field vector was mostly on and parallel to the cavity axis. This minimized any possible trouble due to ion-beam deflection or focusing, although calculations predicted very small effects even for a transverse electric field. Holes had to be drilled for the beam to pass through the cavity; the TM_{020} mode corresponded to a large cavity diameter and was therefore not affected much by holes in its end walls. The hole sizes in the end walls were much larger than the beam sizes there, and hence the walls did not intercept the beam. Note that had we used a $^3He^+$ beam, the microwave prequench technique would not have worked as cleanly, since the hyperfine structure of the $2s_{1/2}$ and the $2p_{1/2}$ states would have split the line into four lines with the different frequencies 14.526, 14.887, 13.443, and 13.804 GHz.[9] Owing to the high Q of the cavity and the klystron monochromaticity, the different hyperfine levels of the $2s$ state would have decayed at different rates. The ion $^4He^+$ does not have hyperfine structure and hence no complications arose.

The whole microwave system is shown in Fig. 2.

C. Translatable $He^+(2s)$ detection assembly

The assembly previously shown in Fig. 4 of paper I required modification; the new arrangement is shown in Fig. 3. The incident and scattered beams entered the detection assembly through a dc $He^+(2s)$ prequench region which was formed by a set of 10 equidistant stainless-steel discs with round apertures. In the following $He^+(2s)$ quench region the electric field between the plates "R" and the grid structure deflected and separated the different charge components of the beam and also quenched the $2s$ state of He^+ by electric field mixing with the $2p$ state whose field-free lifetime is 10^{-10} sec. The 304-Å light emitted in the $2p$-$1s$ decay was viewed by a photomultiplier "Y," while detectors "T" and "U" intercepted the He^+ and He particle beams, respectively, and Faraday cup "S" collected the He^{++} beam.

When the entrance slit "Q" was completely removed, the entrance aperture became circular with a diameter 1.575 ± 0.005 cm.

1. Axial dc electric field $He^+(2s)$ prequench region

The dc prequench region was made from a set of 10 stainless-steel rings with a 2.54-cm i.d., 5.08-cm o.d., and a 0.121-cm thickness. They were separated by 0.635-cm-diam quartz balls, which resulted in an inter-electrode gap of 0.60 cm. Each pair of consecutive rings was connected by a 10-MΩ (±2%) high-temperature carbon-deposited resistor (TRW Model CR-8), and the dc prequench voltage was applied to the central electrode.

A similar arrangement has been used by several investigators to produce uniform electric fields.[10-12] For the present arrangement the nominal uniformity was better than 1% up to 1.25-cm radial distance from the axis. The finite thickness of the rings introduced a 1% sinusoidal oscillation on top of the smooth constant field (Ref. 12, Fig. 5). The influence of the entrance and exit slits was to change the potential by 5% up to one aperture diameter inside the region, causing negligible effects when the aperture was small (0.025 cm). The overall focal length of such an arrangement was about 300 cm for a 1-kV potential on the central electrode and a 10-keV beam.

2. dc electric field $He^+(2s)$ quench region

The dc quench region was formed by a highly polished stainless-steel plate of dimension 2 cm parallel to the beam opposite a tungsten grid of 0.047-cm hole size and 88.4% transmission. The gap or separation between plate and grid was 1.90 ± 0.05 cm. The grid was placed 0.83 cm below the beam axis. The grid was tightly held between two polished stainless-steel plates in such a manner that the grid formed a continuous plane surface with the top plate. The detector could view the quench region through a 2.54 ± 0.03-cm radius hole machined through the grid support assembly. This hole was entirely covered by the grid, and the whole grid assembly was insulated from the rest of the machine by four ceramic pillars. Voltages up to 10 kV were applied to the quench plates "R" with no bad effects such as sparking or rupturing of the grid.

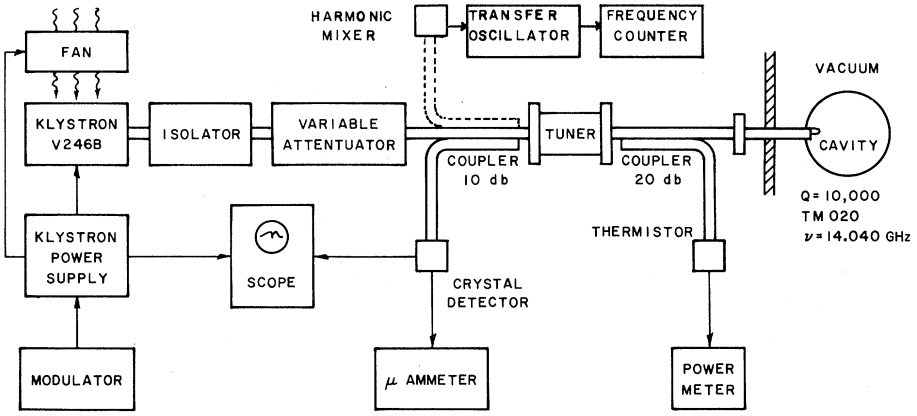

FIG. 2. Schematic diagram of the 14.04-GHz microwave system.

3. He^+ Lyman-α light detector

The critical metastable detection element was the extreme-ultraviolet photomultiplier itself. The principal requirements of such a detector are high quantum efficiency, high gain, stability, large acceptance solid angle, low dark current, reliability, and ease of operation. The detector used was a Johnston Multiplier Model MM-1SB. The MM-1 is a 20-stage focused-mesh secondary-emission electron multiplier using copper-beryllium dynodes, each of which has many cusp-shaped surfaces separated by holes. Adjacent dynodes are separated by ceramic insulators and connected electrically by inter-dynode resistors (1 MΩ).

The advantages of this multiplier include ease of operation, high gain without ion feedback and without afterpulsing, short rise time (to approximately 90% pulse height in 3 nsec), short transit time (approximately 25 nsec), no magnetic or stray fields associated with it, low noise, and last but not least the large active circular surface area (9 cm^2). The multiplier was 3.54-cm long and had an over-all diameter of approximately 5.0 cm.

The whole detector was isolated from machine ground by a 1.5-cm-long ceramic insulator and was shielded all around from stray electrons and light. The detector grid was 1.8 ±0.1-cm below the beam axis, and the detector viewed the quench region through the 88.4% transmission grid assembly. The axis of the viewing aperture was collinear with the axis of the detector, and the center of the quench plate "R" was 0.61 ±0.01 cm down stream from this axis. The quench electrode was so displaced on purpose, so that the MM-1 detector viewed the light from the fringe field of the quench region, where at high collision energies some of the $He^+(2s)$ were quenched (this will be discussed in detail in Sec. III E).

The output from the MM-1 detector was terminated by 93 Ω at the input of a fast-rise-time amplifier. The detection electronics were all commerical, of the NIM nanosecond-pulse type.

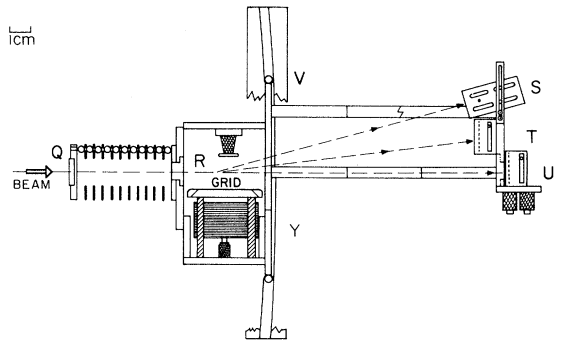

FIG. 3. Schematic diagram of the $He^+(2s)$ detection assembly. Q: entrance aperture of diameter 1.575 ±0.005 cm; R: electrostatic charge analyzing and quenching region; S: positive ion-beam monitoring Faraday-cup assembly; T: positive ion-beam monitoring resistive-strip magnetic particle multiplier, Bendix M-306; U: neutral-beam monitoring resistive-strip magnetic multiplier, Bendix M-306; V: stainless-steel guide rails with 238-cm radius of curvature; Y: $He^+(2s)$ quenching radiation Lyman-α photomultiplier, Johnston MM-1.

D. Data acquisition system

The data acquisition system is shown in Fig. 4. In brief, this system made possible the simultaneous counting of (i) Lyman-α photons "γ" from quenched $He^+(2s)$, (ii) all He^+ ions in the scattered beam, and (iii) that fraction of the He^+ count rate associated with the $He^+(2s)$ state, i.e., in delayed time-coincidence with an associated Lyman-α

channel pulse.[13] The coincidences "C" and accidental coincidences "AC" were simultaneously counted using parallel systems, one with the proper photon-ion time delay and the other at a quite different time delay.

All the above-mentioned signals were measured (a) for the $He^+(2s)$ state prequenched out of the beam by the microwave system, state "PQ," and (b) for the prequenching off, state "$\overline{PQ}$." A precision-time digital lock-in system made possible the observation of very small fractional signals arising from the change in state of the microwave prequencher.

After amplification, pulses from the MM-1 and the M-306 detectors (both about 10-nsec wide) were amplitude selected and counted by fast TSI gateable scalers labeled "γ" and "He^+," respectively. The outputs from the discriminators were also used to drive two time-to-amplitude converters (TAC) connected in parallel. The outputs from the TAC's were amplitude selected by a pair of single-channel analyzers (SCA), with their outputs in turn counted by four gateable Ortec scalers. The output from the TAC's also could be viewed on a multichannel analyzer (MCA), also gateable with the output from the SCA's. When the MCA was gated, it showed the time portion of the TAC output that the scalers were allowed to count by their corresponding SCA's.

All the scalers were gated by a master gating network whose total internal complex is not shown here. Its outputs had the same selectable frequency (up to 1 MHz) and more important the same pulse duration (to within 10 ppm). The network would always give the same finite number of A and B pulses, and the network was gateable by an overflow signal from one of the TSI scalers (usually the scaler that counted the total beam or total time per channel). The pulse lengths of A and B were simultaneously adjustable using a single resistor.

In addition to gating the scalers, the microwaves were also gated by modulating the beam voltage output of the klystron power supply on and off the cavity resonant frequency. A diagram of the gating pulses with the relevant timing is shown in Fig. 5. A delay feature between the clock transition and the scaler gate was necessary on two counts: First, it took the microwaves about 3 μsec to decay or build up; second, owing to the finite speed of the He^+ beam (always faster than 7×10^7 cm/sec) the modulated portion of the $He^+(2s)$ state reached the MM-1 detector after 1 μsec (at most). This limited the modulation frequency (clock frequency) to a maximum of 500 kHz.

III. EXPERIMENTAL PROCEDURES

A. Introduction

The present method of measuring the cross section σ_{21}^* for electron transfer into the $2s$ state of He^+ was based upon first measuring the ratio $K=(\sigma_{21}^*)/(\sigma_{21})$ accurately and later using values of σ_{21} from paper I to obtain values of $\sigma_{21}^*=K\sigma_{21}$. The experimental procedures used to obtain σ_{21}^* will be discussed in this chapter along with auxiliary experiments used to check these procedures and the data. The reader should keep in mind that in every case the atomic-collision signals being discussed are all target-gas-background corrected. This was performed by subtracting every scattered current (or count) with the gas flow "dumped" (or by-passing the target region) from the corresponding scattered current (or count) with the gas in the target.

B. Working equations

The production rate of He^+ ions resulting from the scattering of an He^{++} ion beam of intensity N^{++}

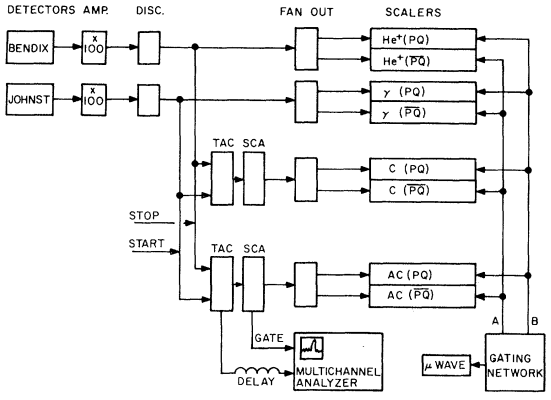

FIG. 4. Data acquisition system.

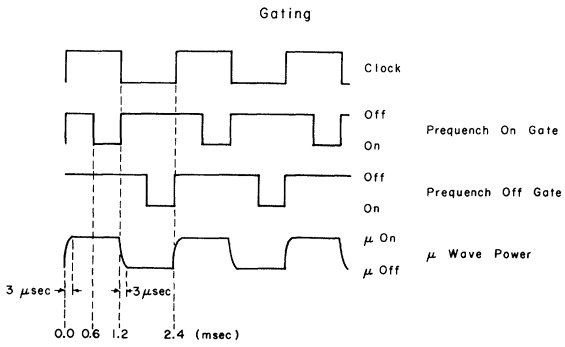

FIG. 5. Schematic diagram of the gating signals.

from a thin target with thickness Π is given by

$$N^+ = N^{++}\sigma_{21}\Pi, \tag{3}$$

where σ_{21} is the cross section for single-electron transfer. The rate of metastable $He^+(2s)$ ion production is similarly

$$N^{+*} = N^{++}\sigma_{21}^*\Pi, \tag{4}$$

where σ_{21}^* is the cross section for single-electron transfer into the $2s$ metastable state of He^+.

When the $He^+(2s)$ ions passed through the dc quench field they were deflected by the negative voltage V_Q on the quench plate "R" and detected by the M-306 particle multiplier with a detection efficiency ϵ_B that includes the efficiency of the electronics as well. The scaler labeled $He^+(\overline{PQ})$ would count

$$He^+(\overline{PQ}) = \epsilon_B N^+ \tag{5}$$

when the prequench voltage was off, and the complementary scaler $He^+(PQ)$ would count

$$He^+(PQ) = \epsilon_B N^+ \tag{6}$$

when the prequench field was on. Any asymmetry between these two scalers would be due to the change of the efficiency of the detector with the internal state of the He^+ ion and/or due to electronic asymmetry. Usually the two scalers agreed to within 0.05%. We define the He^+ signal by the quantity M^+,

$$M^+ = \tfrac{1}{2}[He^+(\overline{PQ}) + He^+(PQ)] = \epsilon_B N^+. \tag{7}$$

The quenching voltage V_Q would also mix the $2s$ state with the short-lived $2p$ state, and an $He^+(2s)$ ion would then radiate a decay photon at 304 Å. The photon was detected by the MM-1 detector with an efficiency ϵ_L, an over-all efficiency that includes all effects. When the prequench field was on, the scaler labeled $\gamma(\overline{PQ})$ counted a background signal. When the prequench field was off, the scaler labeled $\gamma(PQ)$ counted

$$\gamma(PQ) = B + \epsilon_L N^{+*},$$

where B is the background. We define a light signal L by

$$L = \gamma(PQ) - \gamma(\overline{PQ}) = \epsilon_L N^{+*}. \tag{8}$$

Every ion that emitted a photon detected by the MM-1 photomultiplier was an He^+ ion that could hit the M-306 particle multiplier. If a properly time-delayed pulse time-coincidence condition for the photon and its parent ion is imposed, then the coincidence count rates counted by the C scalers would be (see Fig. 4)

$$C(\overline{PQ}) = B + N^{+*}\epsilon_L\epsilon_B + AC(\overline{PQ}), \tag{9}$$

$$C(PQ) = B + AC(PQ), \tag{10}$$

while the accidentals scalers [labeled $AC(\overline{PQ})$ and $AC(PQ)$] counted the accidental rates in the coincidence channels $C(\overline{PQ})$ and $C(PQ)$, respectively. Equation (9) assumes unity coincidence-detection efficiency, that is, that the time window for coincidences is larger that the total time-spread of true coincidence events. This was verified by time-to-pulse-height analysis using the electronics of Sec. IID. We now define another quantity C that corresponds to the true background-corrected and accidentals-corrected coincidence rate

$$C = C(\overline{PQ}) - AC(\overline{PQ}) - [C(PQ) - AC(PQ)] = N^{+*}\epsilon_L\epsilon_B. \tag{11}$$

From the above definitions one obtains the working equations

$$\sigma_{21} = 2e(M^+/I^{++})(1/\Pi)\,L/C \tag{12}$$

and

$$\sigma_{21}^* = \sigma_{21}(1/\epsilon_L)(C/M^+), \tag{13}$$

where I^{++} is the incident He^{++} current and $2e$ is the charge per incident He^{++} nucleus. All the quantities in brackets were measurable, except for ϵ_L. Equations (12) and (13) along with the definitions (7)–(11) were the working formulas relating scaler readings to cross sections.

C. Procedures for taking the data

The angular distribution of the metastable $He^+(2s)$ ions was first measured using the dc prequench field and the small 0.025-cm aperture "Q" on the translatable detector assembly. A scan of the cross-section ratio K for different targets is shown in Fig. 6. Remembering that the angular distribution of the scattered He^+ beam was found to be very sharply peaked in the forward direction (see paper I, Fig. 5), then data such as those in Fig. 6 show that scattering leading to $He^+(2s)$ was mostly within a circle 0.250 cm in diameter, even at the lowest He^{++} energy used. When this energy was increased the angular spreads themselves decreased while the ratio of angular distributions sometimes broadened.

It took quite a long time to measure angular distributions with the small aperture "Q," as less than 1% of the beam was sampled at a time. For measuring total cross sections the small aperture was removed. The resultant effective aperture of diameter 1.585 cm then allowed essentially all of the scattered beams to enter the detection assembly. The beam diameters themselves were observed to be much smaller than the 1.56×1.83-cm cathode area of the M-306 particle multiplier (see paper I).

It was initially hoped that the above dc prequench arrangement for angular distributions would also work very quickly and accurately for measurement of the total cross section σ_{21}^{*}. But unfortunately the required new large aperture contributed its share of troubles. As the dc prequench voltage was scanned or changed, the beam began to show focusing effects. Previous studies had shown that the efficiency of the Bendix M-306 detector varies considerably across the full extent of its cathode surface.[14-16] As a result, the efficiencies of the light and particle detectors changed somewhat with the state of the prequench voltage, and the working equations of Sec. III B did not apply. This trouble was traced to the large perturbing effect on the dc prequench field uniformity of the new large prequench-region beam-entrance and exit apertures. So the dc prequench field was replaced by the fixed microwave prequench cavity of Sec. II B, placed far from the detection region in the fourth vacuum chamber.

The data-taking procedures for an $He^{+}(2s)$ cross-section run were as follows. The energy of the beam was set, and then the beam was mass analyzed, collimated, scattered, and properly steered into the detector assembly using a minimum of electric deflection fields. The quench voltage was then adjusted to simultaneously peak both the He^{++} and He^{+} beams into the Faraday cup and onto the Bendix multiplier, respectively. It was checked that the Faraday-cup reading agreed with that of the "good" Faraday cup labeled "M." Then the TAC output delay-time spectrum was viewed on the multichannel analyzer and the SCA's were adjusted so that the C scalers counted the prequenchable signals and the AC scalers counted the accidentals. Care was taken to adjust the SCA's so that the C and AC scalers viewed equal time ranges. The Faraday-cup output was fed into a Keithley 610 electrometer, whose output was converted into a frequency by the voltage-to-frequency conversion section of a Dymec 2401 digital voltmeter. The resultant frequency was counted by a TSI 100-MHz scaler. The 1-MHz time base of the digital voltmeter was fed to another scaler. Both scalers were gated in the manner of Fig. 5. Usually data were taken for a preset-time or a preset-total He^{++} beam count large enough for the statistical uncertainties in accumulated He^{+} and γ scaler counts to be less than 1%. A data point was repeated many times both with gas in the target and gas dumped outside the target, and with different target gases all at the same target pressure. All such runs at a given beam energy were performed with the same pulse-counting discriminator settings, the same detector voltages, and the same target thicknesses.

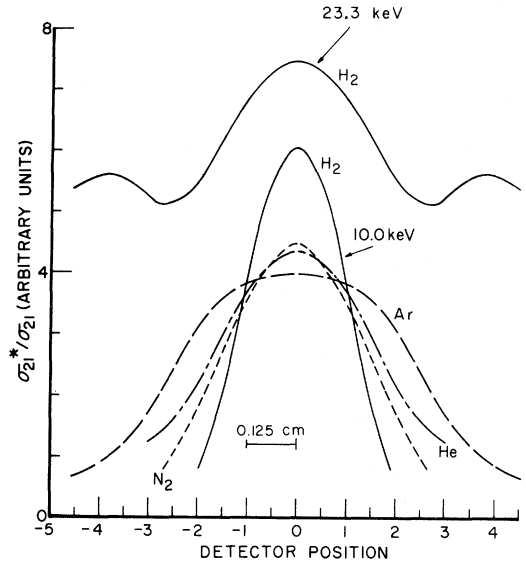

FIG. 6. Fraction of scattered He^{+} in the $2s$ state as a function of scattering angle for He, Ar, H_2 and N_2 targets at 23.3 keV. Each curve has a different arbitrary vertical scale. Two curves for H_2 are displayed, the upper one at 23.3 keV and the lower one at 10 keV. One unit of detector position corresponds to a change in angle of 0.50 mrad. The angular resolution was about 0.05 mrad.

D. $He^{+}(2s)$ prequenching studies

The formulas derived in Sec. III B depend on the fact that prequenching was complete and that no spurious contributions to prequench-defined signals existed. This had to be proven and checked. The two-state theory of Lamb for the $2s$ state in an electromagnetic field of angular-frequency ω and electric field intensity F predicts a lifetime τ_{2s} of the $2s$ state given by[17]

$$\frac{1}{\tau_{2s}} = \frac{1}{\tau_{2p}} \left(\frac{V}{\hbar}\right)^2 \frac{1}{(\omega-\omega_0)^2 + (\frac{1}{2}A)^2}, \tag{14}$$

where

$$A = 10.0\times10^{9}\ \text{sec}^{-1},$$

$$\omega_0 = 14.040\times2\pi\times10^{9}\ \text{rad/sec},$$

$$V/\hbar = 6.96F(\text{V/cm})\ \text{MHz/sec},$$

$$\tau_{2p} = A^{-1} = 10^{-10}\ \text{sec}.$$

Then for a pure dc Stark field we have

$$\frac{1}{\tau_{2s}} = \frac{1}{\tau_{2p}} \left(\frac{F(\text{V/cm})}{12674}\right)^2 = 63\left[F\left(\frac{\text{V}}{\text{cm}}\right)\right]^2 \text{sec}^{-1}, \tag{15}$$

and for a resonant radio-frequency field, $F(t) = F_0\cos\omega t$ and $\omega = \omega_0$, we obtain

$$\frac{1}{\tau_{2s}} = \frac{1}{\tau_{2p}} \left(\frac{F_0(\mathrm{V/cm})}{715}\right)^2$$
$$= 1.96\times10^4 \left[F_0\left(\frac{\mathrm{V}}{\mathrm{cm}}\right)\right]^2 \mathrm{sec}^{-1}. \quad (16)$$

In both cases the lifetime depends on the square of the electric field amplitude. The fraction Q of $2s$ states remaining after a time t in the electric field $F(t)$ is given by

$$Q = \exp\left(-\int_0^t \frac{dt}{\tau_{2s}}\right). \quad (17)$$

When the magnitude of the electric field is experimentally varied the corresponding data should conform to the theoretical predictions of Eq. (17).

For the dc prequench case the electric field had a constant value inside the prequench region equal to $V_{pq}/\frac{1}{2}l$, where $\frac{1}{2}l$ was one-half the length of the prequench region and V_{pq} was the applied prequench voltage. We then have $\log_e Q = -kV_{pq}^2$, where k is a constant (to first order in V_{pq}/U_{acc}, where U_{acc} was the accelerating voltage). Figure 7 shows such an experimental plot of Q vs V_{pq}^2. The tail at large V_{pq}^2 was due to the fact that at large electric fields the lifetimes of the $2s$ state did not follow Eq. (14), but a slightly more complicated formula.[18]

For microwaves the quantity F_0^2 is proportional to the input power to the cavity. Hence a semilog plot of Q versus the input power should also show a linear behavior. Figure 8 shows an example of the data for the coincidence signal C normalized at zero power to unity.

E. $He^+(2s)$ quenching studies and the Lyman-α detector efficiency ϵ_L

A procedure similar to the dc prequench checks was followed here, but as expected it was found that the signal dependence on quench voltage did not obey a simple expression. The reason was that one has to consider the variation in the light collection efficiency as a function of the quenching electric field. The detection efficiency for the light depends on the following spatially dependent quantities: the angular distribution of the emitted light, the photoelectron-emission coefficient of the photomultiplier cathode as a function of position and angle of photon incidence on its surface, and the photoelectron-collection and detection efficiency of the multiplier dynode structure as a function

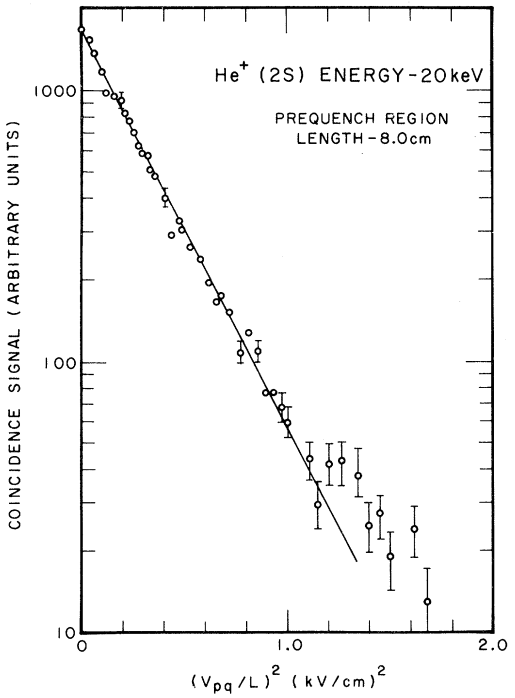

FIG. 7. Metastable $He^+(2s)$ true coincidence signal as a function of the square of the dc prequench electric field. $L = 4$ cm is one-half the nominal length of the prequench region. The prequench voltage used was negative, accelerating the beam and then decelerating it inside the prequench region. The experimental slope of this curve is 3.35 ± 0.1 cm^2/(kV)^2 while a theoretical estimate is 3.75 cm^2/(kV)^2, which includes the effect of field acceleration but not that of field nonuniformity.

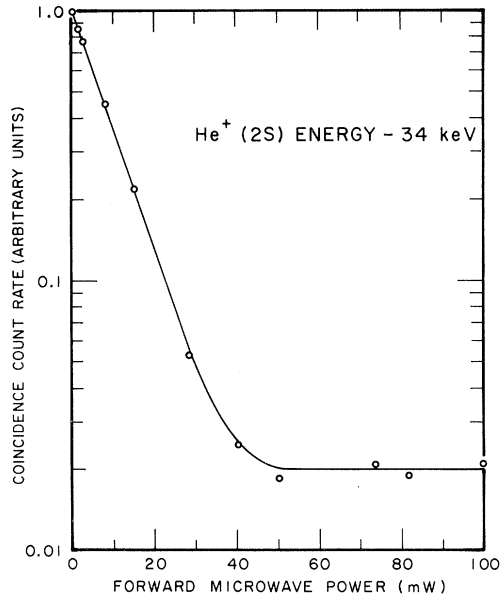

FIG. 8. Metastable $He^+(2s)$ coincidence signal as a function of the prequench microwave cavity input power. Accidental coincidences are not subtracted. A theoretically estimated fraction of $He^+(2s)$ surviving is $e^{-0.115P}$, whereas the experimental data fits the curve $e^{-0.10P}$, P in mW incident microwave power measured on the power meter of Fig. 2.

of position of emission from the surface (or equivalently the change of gain with position on the surface). This last function implicitly depends on the discriminator settings and the consequent electronic efficiency and the transmission function of the grid in front of the detector. The spatial dependence of the electric field must also be accurately taken into account.

Numerical calculations[19] of the quench-field distribution and detector solid-angle effects accurately reproduced all details of the dependence of the $He^+(2s)$ coincidence signal upon the quench-field strength for a wide range of field values. This was found to be a fairly sensitive check for most systematic errors in these quantities. Figure 9 shows a comparison of one such calculation with the data; here both theory and data are normalized to one at a quenching voltage V_Q of 3.5 kV.

The photoelectron emission coefficient for Be-Cu at 304 Å was taken to be 0.065 ± 0.005.[20] An important observation is that 304 Å is a sufficiently short wavelength for surface-contamination effects on the emission coefficient to be small, leading to values reproduced by different investigators.[21] Also, the spread in such coefficients for a wide range of metallic surfaces is only about ±25% centered about the 0.065 value for Be-Cu.[20,21] Thus, the photoelectric secondary-emission problem for He^+ Lyman-α radiation is not as difficult as that for H at 1216 Å.

For each beam energy and the corresponding V_Q actually employed, a value for ϵ_L was calculated. The resultant light-detection efficiency curve is shown in Fig. 10. The shape of the curve reflects the fact that at low energies the quenching electric field is so small that not all the metastables are quenched, while at high energies it is so large that many of the $He^+(2s)$ get quenched in the fringe field where the solid angle subtended by the detector is smaller. The effect of polarization of the Lyman-α radiation emitted in the quenching electric field is not included in this result but is discussed separately below.

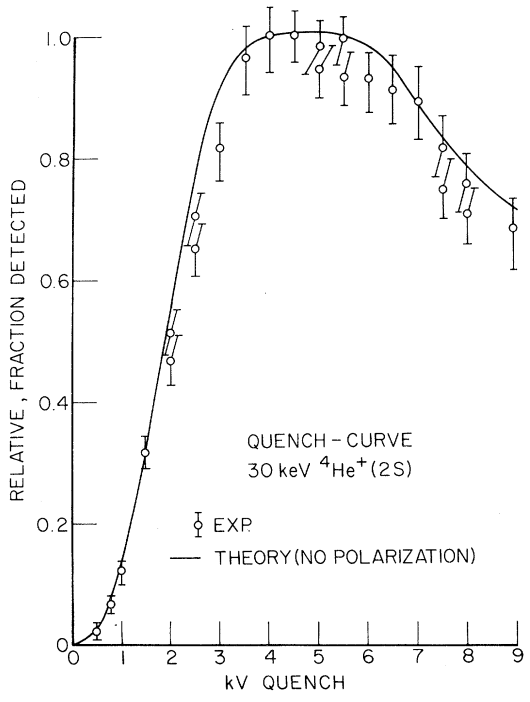

FIG. 9. Quench curve for a 30-keV $^4He^+(2s)$ beam. The experimental and theoretical curves are each normalized to one at 3.5 kV quenching voltage.

F. Polarization of the Lyman-α radiation

If one uses the Schrödinger perturbation treatment to first order, then the amplitudes for the $2P_{3/2}$, $2S_{1/2}$, and $2P_{1/2}$ states are b_1, b_2, and b_3, respectively, given by

$$b_J = \langle J|H_1|2\rangle/(E_2 - E_J), \tag{18}$$

where $H_1 = e\vec{F}\cdot\vec{r}$ and E_2 and E_J are perturbed energies. (This is an approximate modification called the "adiabatic perturbation.") If one takes the energy of the $2P_{1/2}$ state with the electric field $F = 0$ as the zero of energy, then in atomic units we obtain[22]

$$E_1 = \delta, \quad E_2 = \tfrac{1}{2}L + \tfrac{1}{2}\beta, \quad E_3 = \tfrac{1}{2}L - \tfrac{1}{2}\beta, \tag{19}$$

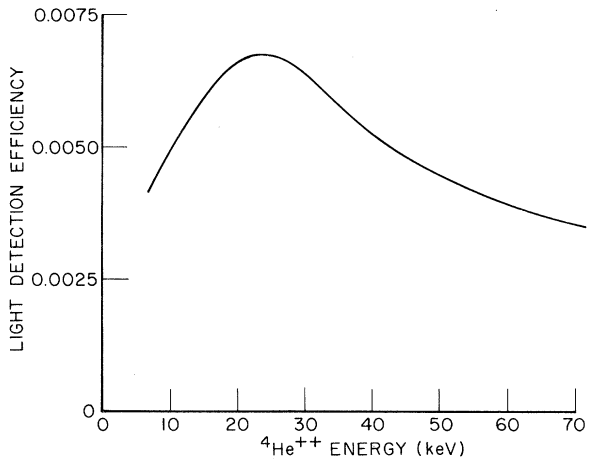

FIG. 10. Light detection efficiency. This curve was calculated for the actual quench voltages used in taking coincidence cross-section data at each energy. A $\sec(\theta)$ law for the secondary-electron emission coefficient was used and the transmittance of the grid was accounted for exactly.

where L is the $2S_{1/2} - 2P_{1/2}$ Lamb shift, δ is the $2P_{1/2} - 2P_{3/2}$ fine-structure interval, and

$$\beta = (L^2 + 12|F/Z|^2)^{1/2}, \tag{20}$$

with $Z = 2$ for He^+. Hence $E_3 - E_2 = -(L + 2\Delta)$, and $E_1 - E_2 = \delta - L - \Delta$, where $\Delta = |\frac{1}{2}(\beta - L)|$ is the magnitude of the Stark shift of the $2S_{1/2}$ as well as the $2P_{1/2}$ state. The polarization P of the decay radiation is defined as

$$P = (I_{\parallel} - I_{\perp})/(I_{\parallel} + I_{\perp}), \tag{21}$$

where $I_{\parallel}$, $I_{\perp}$ are intensities of light components with electric fields parallel and perpendicular to the external electric field direction, respectively. These intensities are related to the amplitudes b_J obtained after evaluating matrix elements[22] to yield

$$P = \frac{b_3^2 + 2b_1^2 + 2\sqrt{2}\, b_1 b_3}{b_3^2 + \frac{1}{2}b_1^2 - 2\sqrt{2}\, b_1 b_3} = \frac{(2G+1)^2 - (G+1)^2}{(2G+1)^2 + (G+1)^2}, \tag{22}$$

where $G = (E_1 - E_2)/(E_3 - E_2)$. Formula (22) reduces to the results of Sellin *et al.*[23] when $Z = 1$.

Figure 11 shows the "adiabatic polarization" P plotted as a function of the static electric field for the quenching radiation from a $^4He^+(2s)$ ion. The polarization varies from -0.2668 at zero field to -1 at extremely large fields.

We now recall that the angular distribution of the radiation

$$I(\theta) = (3/4\pi)(1 - P\cos^2\theta)/(3 - P) \tag{23}$$

is slightly peaked in the $\theta = 0$ direction of the applied external electric field for negative polarization. In the present case where we observe in a direction about parallel to the field, the polarization tends to increase the measured cross section relative to that for completely unpolarized light. Thus the measured cross section tends to be larger than the true cross section by at most 15%, because of the anisotropy of the stimulated Lyman-α decay radiation.

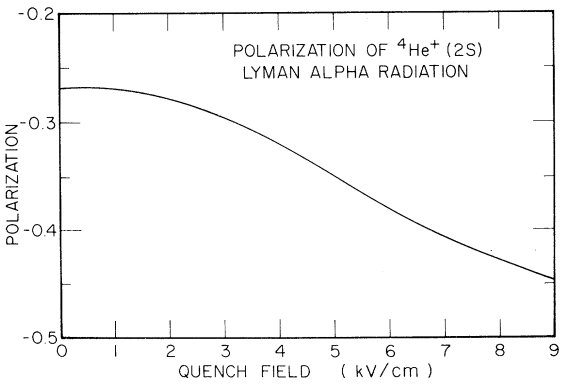

FIG. 11. "Adiabatic" polarization of $He^+(2s)$ quench-induced decay radiation in a static electric field.

IV. RESULTS

The results of the present experiments are shown in Fig. 12. Also shown is the very recent $^3He^{++}$ data of Shah and Gilbody[6] (SG) plotted at equivalent $^4He^{++}$ incident beam energy. These investigators did not mention whether the plotted cross sections were per atom or per molecule, although apparently they are the latter. Qualitative agreement in the energy dependences for the two data sets is generally observed. A further comparison of the two sets was made by evaluating at each energy the ratio $\sigma_{21}^*(X)/\sigma_{21}^*(\mathrm{Ar})$ for the present data and for the data of SG, with the conclusion that the present data for these ratios agree fairly well with the ratios of SG. Thus the conclusion can be drawn that the major difference between the two sets of data is simply a cross-section scale factor of about 3. In view of the much better agreement between investigators for the total electron-transfer cross sections of paper I, the principal cause of disagreement in this paper is likely to be errors in Lyman-α photon-detection efficiency.

Shah and Gilbody believed that their data were accurate to within a factor of 2. The present results have an absolute rms uncertainty of ±35% at the 80% confidence level, with an additional possible +15% correction due to the polarization effect of the stimulated Lyman-α radiation. Major contributions to the quoted rms uncertainty [see Eq. (13)] were due to σ_{21} (taken to be ±20%; see Paper I), the shape of $\epsilon_L(E)$ shown in Fig. 10 (±10%, mainly due to uncertainty in the electric field distribution), and the over-all quantum efficiency of the detector proper (±25%). When all experimental uncertainties are added the lower limits of the present error bars just touch the upper limits of the error bars of SG. But given the limits of the quoted error bars it seems that the best actual unprejudiced cross section values would lie about a factor of 2 above the results of SG and about an amount −35% below present values.

No theoretical results exist for the present $He^+(2s)$ processes except for a continuum distorted-wave calculation by Belkic and Janev[24] for the process $He^{++} + He \rightarrow He^+(2s) + He^+$ at 25 keV. Their predicted cross-section value is 81 Å²/(atom), a value two orders of magnitude larger than that experimentally observed.

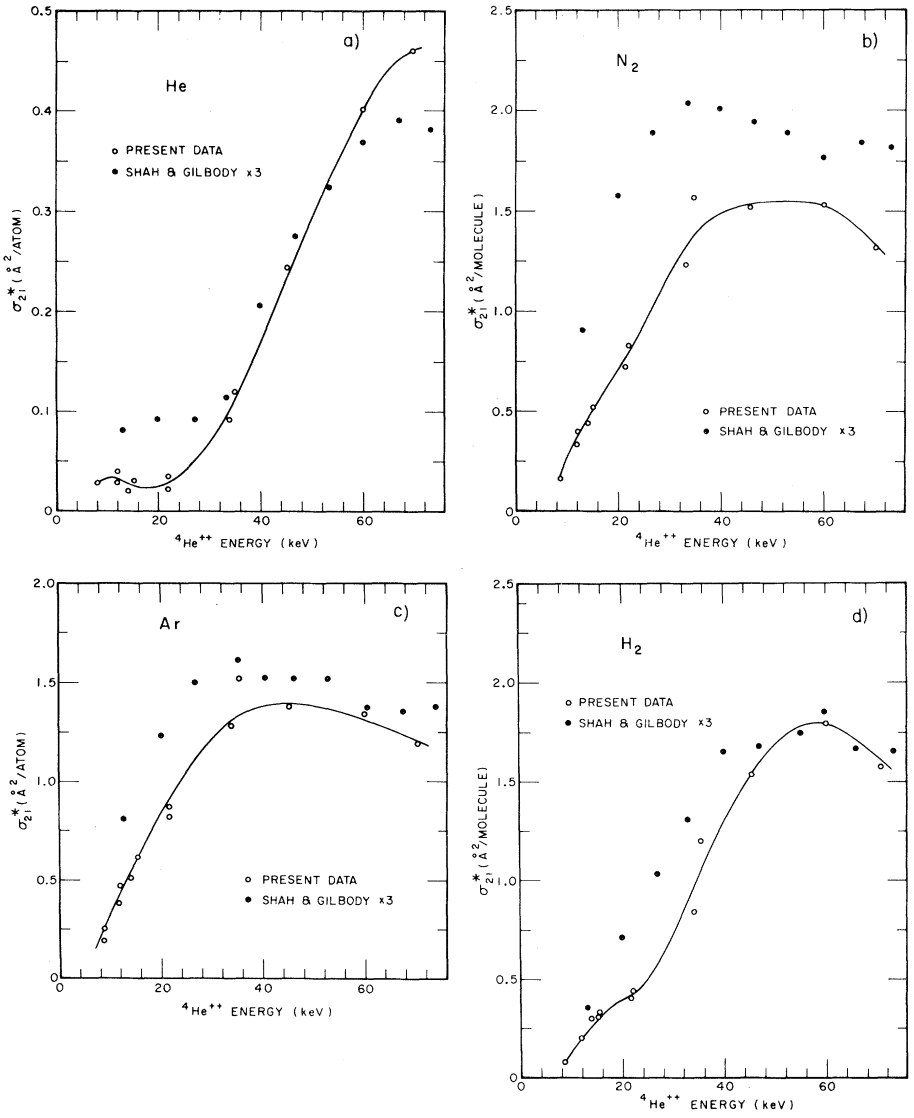

FIG. 12. Cross sections σ_{21}^* for single electron transfer into the 2s state for He^{++} collisions in thin gas targets. (a) Target gas He, (b) N_2, (c) Ar, and (d) H_2. The $^3He^{++}$ data of Shah and Gilbody are plotted at the equivalent $^4He^{++}$ energy where the collision velocities are equal, and are multiplied by 3. Uncertainty in the present data is about ±35%, whereas SG believed their results accurate to within a factor of 2.

We observe that electron transfer into the $n=2$ state of He^+ is an exothermic process for all the collisions studied. Furthermore no potential-energy curve crossings appear to be involved. No general theory has yet been applied to such processes except for the adiabatic criterion. As already discussed in relation to σ_{21} in paper I, the Coulomb repulsion of the nuclei modifies the exit-channel internuclear potential, complicating the application of the adiabatic criterion. The observed cross sections σ_{21}^* all reach maximum values at energies higher than 40 keV. As shown in paper I, this is inconsistent with the adiabatic criterion when using values of ΔE at infinite separation of the nuclei.

When the data of Fig. 12 for σ_{21}^* is divided by the corresponding value of σ_{21} for each gas as given in paper I, the fractional production of He^+ in the 2S state is found to attain values between 3% for He at 20 keV and 17% for He at 60 keV. Values for the other gases are intermediate. These ratios will be compared graphically in paper III with corresponding values for an atomic hydrogen target.

†Work sponsored by the U.S. Air Force Office of Scientific Research, AFSC, under AFOSR Contract No. F44620-71-C-0042.

*Present address: Joint Institute for Laboratory Astrophysics, University of Colorado, Boulder, Colo. 80302.

[1]J. L. McKibben, G. P. Lawrence, and G. G. Ohlsen, Phys. Rev. Lett. 20, 1180 (1968).

[2]W. E. Burcham, O. Karban, S. Oh, and W. B. Powell, Nucl. Instrum. Methods 116, 1 (1974).

[3]J. E. Bayfield and G. A. Khayrallah, preceding paper, Phys. Rev. A 11, 920 (1975).

[4]M. O. Scully, W. H. Louisell, and W. B. McKnight, Proceedings of the Eighth International Quantum Electronics Conference, San Francisco, 1974 (unpublished).

[5]P. B. Kramer, S. R. Lundeen, B. O. Clark, and F. M. Pipkin, Phys. Rev. Lett. 32, 635 (1974).

[6]M. B. Shah and H. B. Gilbody, J. Phys. B 7, 256 (1974).

[7]J. E. Bayfield and G. A. Khayrallah, Bull. Am. Phys. Soc. 18, 1516 (1973).

[8]J. C. Slater, Rev. Mod. Phys. 18, 441 (1946).

[9]R. Novick and E. D. Commins, Phys. Rev. 111, 822 (1958).

[10]R. W. Crompton, M. T. Elford, and J. Gascoigne, Aust. J. Phys. 18, 409 (1965).

[11]D. L. Albriton, D. W. Martin, E. W. McDaniel, T. M. Miller, and J. T. Mosley, Technical Report, Georgia Institute of Technology, 1967 (unpublished).

[12]P. H. Rose, A. Galejs, and L. Peck, Nucl. Instrum. Methods 31, 262 (1964).

[13]R. H. McKnight, D. H. Crandall, and D. H. Jaecks, Rev. Sci. Instrum. 41, 1282 (1970).

[14]J. E. Bayfield, G. A. Khayrallah, and P. M. Koch, Phys. Rev. A 9, 209 (1974).

[15]H. Neddermeyer, Appl. Opt. 10, 1976 (1971).

[16]L. Heroux, Appl. Opt. 7, 2351 (1968).

[17]W. E. Lamb and R. C. Rutherford, Phys. Rev. 79, 41 (1950).

[18]H. A. Bethe and E. E. Salpeter, *Quantum Mechanics of One- and Two-Electron Systems* (Springer, Berlin, 1957), Sec. 67.

[19]G. A. Khayrallah, Ph.D. dissertation (Yale University, 1974) (unpublished). (Available at University Microfilms, Ann Arbor, Mich.).

[20]R. B. Cairns and J. A. R. Samson, J. Opt. Soc. Am. 56, 1568 (1966).

[21]J. A. R. Samson, *Techniques of Vacuum Ultraviolet Spectroscopy* (Wiley, New York, 1967), Sec. 7.3.

[22]Reference 18, Sec. 55.

[23]I. A. Sellin, J. A. Biggerstaff, and P. M. Griffin, Phys. Rev. A 2, 423 (1970).

[24]D. S. Belkic and R. K. Janev, J. Phys. B 6, 1020 (1973).